The Envelope Kinematics and a Possible Disk Around the Class 0 Protostar within BHR7

John J. Tobin[1,2], Steven P. Bos[2], Michael M. Dunham[3,4], Tyler L. Bourke[5], Nienke van der Marel[6]

ABSTRACT

We present a characterization of the protostar embedded within the BHR7 dark cloud, based on both photometric measurements from the near-infrared to millimeter and interferometric continuum and molecular line observations at millimeter wavelengths. We find that this protostar is a Class 0 system, the youngest class of protostars, measuring its bolometric temperature to be 50.5 K, with a bolometric luminosity of 9.3 L$_\odot$. The near-infrared and *Spitzer* imaging show a prominent dark lane from dust extinction separating clear bipolar outflow cavities. Observations of ^{13}CO ($J = 2 \rightarrow 1$), C^{18}O ($J = 2 \rightarrow 1$), and other molecular lines with the Submillimeter Array (SMA) exhibit a clear rotation signature on scales <1300 AU. The rotation can be traced to an inner radius of ∼170 AU and the rotation curve is consistent with an R^{-1} profile, implying that angular momentum is being conserved. Observations of the 1.3 mm dust continuum with the SMA reveal a resolved continuum source, extended in the direction of the dark lane, orthogonal to the outflow. The deconvolved size of the continuum indicates a radius of ∼100 AU for the continuum source at the assumed distance of 400 pc. The visibility amplitude profile of the continuum emission cannot be reproduced by an envelope alone and needs a compact component. Thus, we posit that the resolved continuum source could be tracing a Keplerian

[1]Homer L. Dodge Department of Physics and Astronomy, University of Oklahoma, 440 W. Brooks Street, Norman, OK 73019, USA

[2]Leiden Observatory, Leiden University, P.O. Box 9513, 2300-RA Leiden, The Netherlands

[3]Department of Physics, State University of New York Fredonia, Fredonia, New York 14063, USA

[4]Harvard-Smithsonian Center for Astrophysics, 60 Garden St., Cambridge, MA, USA

[5]SKA Organization, Jodrell Bank Observatory, Lower Withington, Macclesfield, Cheshire SK11 9DL, UK

[6]Institute for Astronomy, University of Hawaii, 2680 Woodlawn Drive, 96822 Honolulu, HI, USA

[7]Herzberg Astronomy & Astrophysics Programs, National Research Council of Canada, 5017 West Saanich Road, Victoria, BC, Canada V9E 2E7

disk in this very young system. If we assume that the continuum radius traces a Keplerian disk (R∼120 AU) the observed rotation profile is consistent with a protostar mass of 1.0 $M_\odot$.

1. Introduction

The formation of rotationally-supported disks during star formation is a crucial part of the star and planet formation process. Once a disk has formed, stellar mass assembly will then be governed by accretion through the disk, and the disk will further enable the growth of solids, catalyzing the planet formation process (Testi et al. 2014). Furthermore, if the forming disks are sufficiently massive they may fragment via gravitational instability, leading to the formation of a close binary star system or possibly giant planets (e.g., Kratter et al. 2010; Tobin et al. 2016). Also, clumps formed via gravitational instability may lead to episodic bursts of accretion (Vorobyov & Basu 2006), and they may lead to disk snowline radii moving in and out during the protostellar phase (Cieza et al. 2016). However, it is uncertain if (or how often) processes such as gravitational instability can function in protostellar disks because their general properties such as radii, mass, and temperature structure have yet to be characterized for a broad sample. This is because the continuum and molecular line emission of the envelope is entangled with that of the disk early in the star formation process, the Class 0 phase (André et al. 1993; Dunham et al. 2014), when the infalling envelopes are very dense.

In order to understand the formation and evolution of disks, they must be observed throughout the star formation process. Thus, both high spatial and spectral resolution must be coupled with high-sensitivity observations to distinguish the disk from the infalling envelopes. A few examples of disks in Class 0 systems have been found (Tobin et al. 2012b; Murillo & Lai 2013; Ohashi et al. 2014; Codella et al. 2014; Lee et al. 2014; Lindberg et al. 2014; Yen et al. 2015, 2017), having a wide variety of sizes, from >100 AU to <10 AU. However, the total number of systems is still quite small, therefore detections and/or evidence of disks in additional systems are important.

BHR7 (Bourke et al. 1995a) is an isolated dark cloud harboring an embedded protostar, discovered by the coincidence of its mid to far-infrared emission detected by the Infrared Astronomy Satellite (IRAS 08124-3422), an optical dark cloud (Hartley et al. 1986), and ammonia emission (Bourke et al. 1995b). The isolated nature of BHR7 makes it an ideal target to examine, free of confusion from the superposition of neighboring protostars. However, a drawback of an isolated system is its uncertain distance, because of the difficulty to relate BHR7 to a particular star forming region. BHR7, however, is associated with the

Vela Cometary globules and the distance estimates range between 400 pc to 500 pc (Woermann et al. 2001). The systemic velocity of BHR7 indicates that it is on the near-side of an expanding shell, thus we adopt ∼400 pc as the distance to BHR7 throughout the text. In order to distinguish between the protostar and the dark cloud, we will refer to the protostar as BHR7-MMS and refer to the region around the protostar as BHR7.

Since the original detection, this protostar has received little attention in the form of follow-up observations. However, the Two-Micron All Sky Survey (2MASS; Skrutskie et al. 2006) and Santos et al. (1998) observed BHR7 and detected evidence of a bipolar scattered light nebula at 2.15 μm, indicating the possible presence of outflow activity from this source. The bipolar nebula also appeared as if it might be near edge-on in both sets of near-infrared observations from the dark lane that appears to bisect the nebula. Edge-on protostars systems can be advantageous because the orientation enables a clear view of the kinematics, well-separated from the outflow, and any velocity corrections due to inclination are inherently small.

Here we present a multi-wavelength and multi-scale examination of BHR7 using ground and space-based observations spanning the near-infrared to millimeter wavelengths, confirming the evolutionary state of BHR7-MMS as a Class 0 protostar. We subsequently obtained observations with the Submillimeter Array (SMA; Ho et al. 2004) in multiple configurations, gaining both a small-scale (sub-arcsecond) view, and a larger-scale (several arcsecond) view of the kinematic structure. The key advance is that the SMA observations have enabled us to assess the likelihood of a disk in this protostar system. The paper is structured as follows: the observations and data reduction are presented in Section 2, we discuss the overall infrared imaging, spectral energy distribution (SED), and results from the SMA observations in Section 3, discussion of the results is presented in Section 5, and the Summary and Conclusions are given in Section 5.

2. Observations and Data Reduction

2.1. SMA Observations

The SMA is located on Mauna Kea on the island of Hawaii at an altitude of 4000 m, and it nominally has eight 6 meter antennas combined to form the interferometer. BHR7-MMS was observed by the SMA several times during 2015 and 2016 in Very Extended, Extended, and Compact configuration at 1.3 mm; the observations are summarized in Table 1 and detailed in the following sections.

2.1.1. Very Extended Observations

The Very Extended observations were conducted on 2015 January 28 with 6 antennas operating and a maximum baseline of 362 m. The zenith atmospheric optical depth at 225 GHz was ~0.06 throughout the observation. The observation used the ASIC correlator configured for continuum observations, sampling a total bandwidth of 8 GHz (upper and lower sided bands). The spectral resolution was set to 64 channels per 104 MHz spectral chunk and the central frequency was 225.5 GHz. The observations used Callisto as the absolute flux calibrator, 3C279 as the bandpass calibrator, and 0747-331 was used as the complex gain calibrator. The observations were conducted in a standard loop observing the gain calibrator for 3 minutes and BHR7-MMS for 10 minutes. The total time on source was approximately 4.0 hrs.

2.1.2. Compact Array Observations

The Compact array observations were conducted on 2015 December 25 with 8 antennas operating and a maximum baseline of 69 m. The zenith atmospheric optical depth at 225 GHz was ~0.07 throughout the observation. For these observations, Uranus was used as the absolute flux calibrator, 3C84 was the bandpass calibrator, and 0747-331 was the complex gain calibrator. The observations were conducted in a standard loop observing the gain calibrator for 3 minutes and BHR7-MMS for 15 minutes. The total time on source was approximately 5.0 hrs. The correlator was configured for both spectral line and continuum observations with a central frequency of 225.4 GHz; we observed ^{12}CO, ^{13}CO, C^{18}O ($J = 2 \rightarrow 1$), H$_2$CO ($J = 3_{0,3} \rightarrow 2_{0,2}$), and N$_2D^+$ ($J = 3 \rightarrow 2$). All lines had a spectral resolution of 200 kHz (0.26 km s^{-1}), except C^{18}O and N$_2$D$^+$ which had a spectral resolution of 100 kHz (~0.13 km s^{-1}). The total continuum bandwidth was 5.2 GHz (upper and lower sidebands combined).

2.1.3. Extended Array Observations

The Extended array observations were conducted on 2016 April 02 with 8 antennas operating and a maximum baseline of 181 m. The zenith atmospheric optical depth at 225 GHz was ~0.04 throughout the observation. For these observations, Ganymede was used as the absolute flux calibrator, 3C273 was the bandpass calibrator, and 0747-331 was the complex gain calibrator. The observations were conducted in a standard loop observing the gain calibrator for 3 minutes and BHR7-MMS for 15 minutes. The total time on source was

approximately 4.2 hrs. The correlator was configured for both spectral line and continuum observations; it has the same configuration and spectral resolution as the Compact observations, except that H_2CO ($J = 3_{2,1} \rightarrow 2_{2,1}$), SO ($J_N = 5_6 \rightarrow 4_5$), and SiO ($J = 5 \rightarrow 4$) were also observed. They were not observed in the Compact observations due to a correlator problem. The SiO ($J = 5 \rightarrow 4$) transition was also covered at the continuum spectral resolution (1.625 MHz or 2.25 km s^{-1}). The total continuum bandwidth was 10.8 GHz (upper and lower sidebands combined; 5.2 GHz from the original correlator and 5.6 GHz from the early SWARM correlator).

2.1.4. Data Reduction

The SMA data were calibrated and edited using standard techniques within the MIR software package. MIR is an IDL-based software package originally developed for the Owens Valley Radio, Observatory and adapted by the SMA group. We performed subsequent imaging in MIRIAD (Multichannel Image Reconstruction, Image Analysis and Display; Sault et al. 1995) for both the spectral line and continuum data. However, we did import the Very Extended data into CASA (McMullin et al. 2007) for self-calibration. We did this by first exporting the continuum visibility data from MIR to MIRIAD format, then converting the MIRIAD visibility files to UVFITS via the MIRIAD task *fits*, and then importing the data into CASA using the *importuvfits* task. The purpose of using CASA was to perform self-calibration on the continuum, using the procedures established for VLA and ALMA data. The final images from Very Extended were generated in CASA using the *clean* task. Self-calibration of the Very Extended data was useful given that the initial signal-to-noise (S/N) was 50 and phase-only self-calibration on 5 minute solution intervals increased the S/N to >100. The absolute flux density accuracy is between estimated to be between 10–20%.

2.2. Herschel Observations

BHR7 was observed with the *Herschel Space Observatory* as part of the Hi-Gal2π project (OT2_smolinar_7), obsids 1342254511 and 1342254512, using the Spectral and Photometric Imaging Receiver (SPIRE) (Griffin et al. 2010). While these data were acquired in a parallel mode where SPIRE and the Photoconductor Array Camera and Spectrometer (PACS; Poglitsch et al. 2010) observed simultaneously, the PACS coverage missed BHR7 by a few arcminutes. Therefore, BHR7 was only observed by SPIRE at 250, 350, and 500 μm. We used the Jscan imaging products from the archive for photometry. We measured the flux density in a circular aperture around BHR7 with a radius of 40″ and subtracted the background mea-

sured from a nearby region of blank sky. The background region was at RA=8:14:20.390, Dec=-34:36:26.29 and had a radius of $129''$. We used the median background value, and scaled this to the area of the $40''$ aperture. BHR7 is an isolated globule, so extended, diffuse emission from a surrounding cloud was not present, but there is an extended tail to the cloud, prohibiting the use of a background annulus. We used the extended source photometry methods described in the SPIRE data handbook[1], using the extended source color correction factor and aperture corrections. We use values corresponding to a modified blackbody with β=1.5, and a temperature of 30 K; these values are reasonably representative of the SED of the protostar that peaks near 100 μm. The *Herschel* SPIRE photometry are listed in Table 2; the uncertainties given are statistical only, accounting for the RMS noise in the image and the number of pixels summed to measure the flux density. The PACS and SPIRE absolute photometric accuracy are estimated to be 3-5%[2] and 4%[3], respectively. However, in the SPIRE bands there is additional extended emission that we do not capture with the apertures used; thus, the submillimeter flux densities may be systematically low.

2.3. Spitzer Observations

BHR7 was observed with the Infrared Array Camera (IRAC; Fazio et al. 2004) onboard the *Spitzer Space Telescope* on 2008 December 22 as part of program 50477 (PI: Bourke) during the cryogenic portion of the mission. This program observed BHR7 at 3.6, 4.5, 5.8, and 8.0 μm. Using the pipeline-processed images from the *Spitzer* Heritage Archive, we measured the photometry in the IRAC bands using a circular aperture radius of $25''$ ($\sim$10000 AU) and calculated the background using the median of an off-source patch of sky. The *Spitzer* photometry are listed in Table 2.

2.4. CTIO Near-Infrared Observations

BHR7 was observed at Cerro-Tololo Inter-American Observatory (CTIO) on 2009 June 11 using the Infrared SidePort Imager (ISPI; van der Bliek et al. 2004) on the Blanco 4 m telescope. The conditions during the observations were photometric and the seeing was $\sim0\rlap{.}''9$. ISPI provides a $\sim10'$ field of view on a 2048$\times$2048 detector array. We observed BHR7

---

[1]http://herschel.esac.esa.int/Docs/SPIRE/spire_handbook.pdf

[2]http://herschel.esac.esa.int/Docs/PACS/html/pacs_om.html

[3]http://herschel.esac.esa.int/Docs/SPIRE/html/spire_om.html

in J (1.25 μm), H (1.6 μm), and Ks (2.15 μm) bands The observations were conducted in a 10-point box dither patter with a dither step size of 60″. At each position in the dither, 4 × 15s coadds were taken in H and Ks-bands and 2 × 30s coadds in J-band. The sky background was measured using a median combination of the dithered frames; the step size of 60″ preserved extended emission on this scale. A total integration time on source was 40 minutes for J-band, 20 minutes for H-band, and 30 minutes for Ks-band. Further details that discuss the combination of the individual frames to make the final mosaic are given in Tobin et al. (2010c). The data were calibrated using the 2MASS photometry catalog (Skrutskie et al. 2006) and the photometry are listed in Table 2 and are extracted from the same aperture radius as the *Spitzer* IRAC data.

2.5.   Swedish-ESO Submillimetre Telescope Observations

The 1.2 mm (250 GHz) continuum observations were carried out with the 37 channel bolometer array SIMBA (SEST IMaging Bolometer Array) at the SEST (Swedish-ESO Submillimetre Telescope) on La Silla, Chile, between June 2001 and August 2003, as part of a larger program to map the BHR (Bourke et al. 1995a) and Spitzer c2d cores (Evans et al. 2003; Kämpgen et al. 2004). The observations were obtained in fast-scanning mode (80″ per second), with multiple maps obtained at different orientations (hour angles), to reduce artifacts due to the mapping scheme. To estimate the atmospheric opacity sky-dips were undertaken about every three hours. The resulting zenith opacity values were 0.10-0.45. The beam size of an individual SIMBA bolometer was 24″ FWHM, and the positional accuracy was estimated to be 2-3″ from frequent pointing scans on Centaurus A, η Carina, and Uranus. Flux calibration was determined to be accurate to about 10%, through maps of Uranus and Neptune. The RMS at the map center is estimated to be 18 mJy/beam. All data were reduced and analyzed with the MOPSI software according to the instructions of the SIMBA Observer's Handbook (2002)[4] and Kämpgen (2002).

3.   Results

The synthesis of the multi-wavelength dataset collected toward BHR7-MMS has enabled us to characterize the orientation, evolutionary state, luminosity, and the small-scale physical and kinematic structure. All these data together contribute to a much better understanding of this system as an important test case for star formation theories.

---

[4]http://www.apex-telescope.org/sest/html/internal-access/OnlineManuals/Receivers/Simba/simba.ps

3.1.   Near-IR, *Spitzer*, and *Herschel* Imaging

The near-infrared image with sub-arcsecond seeing and the *Spitzer* IRAC imaging shown in Figure 1 reveal the appearance of a prominent bipolar outflow cavity viewed in scattered light from a central illuminating source (the protostar and disk) (e.g., Whitney et al. 2003b). The system has a similar morphology in both its SED and images, to proto-typical Class 0 protostars like L1527 IRS, B335, and L1157 (Tobin et al. 2008; Stutz et al. 2009; Looney et al. 2007), all of which are viewed near edge-on. However, toward BHR7-MMS there is no point-like source visible between the outflow cavities as in L1527 IRS, which was due to scattered light from its edge-on disk (Tobin et al. 2010a). Moreover, BHR7-MMS exhibits a brightness asymmetry with respect to the north and south cavities. The dark lane that is apparent from the near-infrared to 8 μm, the two clearly defined scattered light cavities, and the SED shape indicate that the protostar most likely viewed at an inclination $> 60°$ but $< 90°$ (Whitney et al. 2003a). It is difficult to more precisely determine the inclination from the SEDs and images alone due to degeneracies and asymmetry of the envelope (Furlan et al. 2016). Finally, there are two prominent, apparently symmetric shock knots located in the center of the outflow cavities. These knots are brightest in Ks and 4.5 μm due to the presence of a shock-excited H_2 emission line within these bands. The symmetry of these knots is quite striking, they are both located at a distance of 10″9 ($\sim$4360 AU), indicating a near simultaneous ejection.

The extinction lane in the near-infrared image appears to have a different position angle with respect to the dark lane in the IRAC images. This likely reflects some degree of morphological complexity in the surrounding envelope (e.g., Tobin et al. 2010b); there is also a hint of 8 μm absorption from the surrounding envelope against the mid-infrared background. However, it is also clear that the system is externally illuminated, likely from a ultraviolet emitting source because of the limb-brightened 8 μm emission that is likely from polycyclic aromatic hydrocarbons (PAHs).

We show the *Herschel* SPIRE data in Figure 2 over a larger field that encompasses the dense core where the protostar is forming and a lower density tail extending north. We also show a view of the same field in the near-infrared and there is diffuse scattered light associated with some of the extended submillimeter emission. This view also shows that the cloud is extended in the direction of the outflow and that BHR7-MMS has formed at the end of this filamentary structure.

3.2. Spectral Energy Distribution

Using the near-infrared, *Spitzer* IRAC, IRAS, SPIRE, and SEST SIMBA data, we constructed the SED of this source in order to determine its evolutionary state and plot the SED in Figure 3. We measure a bolometric luminosity of 9.3 $L_\odot$, a bolometric temperature (T_{bol}) of 50.5 K, and a ratio of submillimeter to bolometric luminosity (L_{bol}) of 0.034. Both of these measurements require integrating the SED for which we use the *tsum* procedure from the IDL Astronomy library that integrates the SED using trapezoidal integration. These values indicate that BHR7-MMS is a Class 0 protostar, having both $T_{bol} < 70$ K and $L_{submm}/L_{bol} > 0.005$ (Chen et al. 1995; André et al. 1993); both of these metrics are independent of distance. Furthermore, L_{bol} is significantly above the median for Class 0 protostars, near the top-end of the distribution for low-mass systems (Dunham et al. 2014; Fischer et al. 2017).

3.3. Molecular Line Kinematics

The SED reveals that this protostar is very young, but molecular lines are key to characterizing the kinematics of the envelope in order to determine if there is significant rotation or if it is dominated by infall motion alone. An isolated Class 0 source with an inclination of >60° is an ideal candidate to examine the kinematic properties of the infalling envelope. The lack of nearby sources and the clear geometric orientation simplify the interpretation of molecular line kinematic data. The observations in Extended and Compact configuration were set-up for the mapping of kinematic tracers of the inner envelope (^{13}CO, C^{18}O, and H$_2$CO), outer-envelope (H$_2$CO and N$_2$D$^+$), disk (^{13}CO, C^{18}O), and outflow (^{12}CO).

3.3.1. The Inner Envelope

To evaluate the molecular line kinematics, we utilize both moment maps made for the red and blue-shifted emission, but also by plotting the position and velocity of the molecular line(s). The position-velocity (PV) diagrams of the various molecular line emission are all made with a PV cut in exactly the east-west direction. The PV diagram is made by collapsing one spatial axis on to the other, summing a strip of specified width, thereby transforming the 3D datacube (position-position-velocity) into a 2D image (position-velocity). While this position angle of the PV cut (90° east of north) is not exactly orthogonal to the outflow (off by 5.9°, see Section 3.8), the PV cut direction matches the blue and red-shifted emission peaks of the various molecules.

We show the moment zero (integrated intensity) maps for ^{13}CO and C^{18}O from the combined Compact and Extended configuration data in Figure 4. The integrated intensity maps for the blue and red-shifted ^{13}CO and C^{18}O emission clearly show a position shift between the blue and the red on scales <1300 AU. The PV diagrams shown in Figure 4 offer more detail on the kinematic structure of the emission. The PV diagrams show clearly separated blue- and red-shifted components for both ^{13}CO and C^{18}O, and both molecular lines are resolved out around the source velocity. The lower-velocity emission is observed to extend to larger radii and at a given offset there is a trend for either blue or red-shifted emission to dominate; this is a clear indication of envelope rotation. There is sometimes both blue and red-shifted emission at a given position. The super position of both blue and red-shifted emission at the same position is indicative of radial infall motion in an axi-symmetric system (Tobin et al. 2012a; Sakai et al. 2014). We also notice that toward the source position there is higher velocity emission evident in both ^{13}CO and C^{18}O. Given that there is an indication of rotation at larger radii, this feature likely reflects the increased rotation velocity (or spin-up) of infalling material due to conservation of angular momentum.

To examine the increased velocity or spin-up observed at smaller radii, we make the same blue and red-shifted integrated intensity maps from the Extended configuration data only, see Figure 5. The same general features are observed for the high-resolution data as the low-resolution, but on smaller scales. The higher resolution results in more large-scale emission being filtered-out and the compact emission toward the source is more prominent. In the PV diagrams, the ^{13}CO emission prominently shows the increased velocity at small radii. The C^{18}O shows these features as well, but with lower S/N. These data will be analyzed in more detail in Section 3.4.

In addition to the CO isotopologues, we also examined the H$_2$CO and SO molecular lines for indications of kinematic structure on the scale of the inner envelope and disk. Sakai et al. (2014) detected SO toward L1527 IRS that could be tracing an accretion shock in the outer disk and H$_2$CO traced both the inner infalling envelope and disk. The H$_2$CO emission shows a clear velocity gradient from the blue and red-shifted integrated intensity maps shown in Figure 6; however, the PV diagram does not show the same high-velocity features toward the source position observed in the CO isotopologues (Figure 5). The PV diagram shows a relatively linear change in velocity with position in the PV diagram, with some superposition of both red and blue shifted emission at a given position. Furthermore, less emission is resolved-out at line center indicating that H$_2$CO emission is mainly coming from the inner envelope and there is not significant large-scale H$_2$CO emission in the surrounding globule.

SO emission is detected at small radii and near the source velocity as shown in Figure

6. The integrated intensities are low, such that a separated blue and red-shifted integrated intensity map is not practical to generate. The brightest SO emission being near line-center is consistent with the observations of L1527; however, there is a slight extension (beyond what is expected from the beam) along the direction of the outflow rather than orthogonal to it. While we cannot completely rule-out an outflow shock component, an outflow shock is not expected to produce emission at the source velocity without a higher velocity component. Thus, we cannot firmly associate the SO emission of BHR7 to originate from small-scales like L1527 at the resolution and sensitivity of the data in hand.

3.3.2. Outer Envelope

In addition to the probes of the inner envelope, we also observed N_2D^+ ($J = 3 \rightarrow 2$), a tracer of cold dense gas (Crapsi et al. 2004; Emprechtinger et al. 2009; Tobin et al. 2013). The N_2D^+ transitions, like the more abundant N_2H^+ molecule, have hyperfine structure. However, in the ($J = 3 \rightarrow 2$) transition, many of the brightest hyperfine lines are at similar frequencies, and we only detect the main, blended lines well with the SMA and not the weaker, more widely separated hyperfine lines. We show integrated intensity maps of the N_2D^+ emission in Figure 7, overlaid on the 1.3 mm continuum and near-infrared images. The emission is clearly coming from larger scales than the CO isotopologues, H_2CO, and SO emission. The PV diagram shows that there is a velocity gradient in the outer envelope that connects with the inner envelope velocities probed by the CO isotopologues and H_2CO. The velocity gradient could reflect rotation on this scale, but it has also been proposed that large-scale velocity gradients could also reflect infall of asymmetric envelope structures (Tobin et al. 2011, 2012a).

The N_2D^+ appears to follow the direction of the dark lane observed in the near-infrared and it has a deficit of emission toward the protostar position. The deficit is expected because N_2D^+ (and N_2H^+) is destroyed by efficient reactions with gas-phase CO (Caselli et al. 1999; Bergin et al. 2001; Jørgensen 2004). The presence of gas-phase CO toward the inner regions of the envelope around BHR7-MMS is clear from Figures 4 & 5. Moreover, temperatures around and above the sublimation point of CO will also inhibit the formation of N_2D^+ by reversing the reaction that forms H_2D^+, the key molecule for low-temperature deuterium chemistry (e.g., Langer 1985). The observed morphology of N_2D^+ resembles other protostars with resolved observations of this molecule (e.g., L1157; Tobin et al. 2013), but the N_2D^+ emission peaks on either side of the protostar do not appear to be as symmetric as in L1157. The asymmetry could result from an asymmetric distribution of envelope material around the protostar.

3.4. Rotation Curve Analysis

While the signature of rotation is evident in the ^{13}CO and C^{18}O moment maps and PV diagrams, further analysis is necessary to determine the radial dependence of the rotation curve. This will enable us to determine if the rotation curve reflects conservation of angular momentum (v $\propto$ R^{-1}), Keplerian rotation (v $\propto$ R$^{-0.5}$), or both on different spatial scales. To examine the rotation curve, we measure the position of the ^{13}CO and C^{18}O intensity peaks in each velocity channel by fitting a 2D Gaussian. We only select channels with S/N > 4 and where the emission is not extended more than $\sim$3 resolution elements, enabling the emission peak to be traced as a function of radius. We have plotted the results with their associated velocities (relative to the source) in log-log space, yielding a more quantitative means to evaluate the kinematic structure (e.g. Tobin et al. 2012b; Yen et al. 2013; Ohashi et al. 2014). We refer to this plot as the Peak PV-diagram. The Peak PV-diagram derived from the high resolution ^{13}CO and C^{18}O data (see Figures 4 and 5) is shown in Figure 8. As the data points lie on a line in log-log space, we fitted a power-law using a Monte Carlo simulation and the least-squares fitting algorithm. The power of the best fit is -1.02 $\pm$ 0.04, consistent with material rotating with conserved angular momentum down to a radius of $\sim$170 AU, the smallest radial displacement measured in the molecular line data. Thus, we cannot identify a Keplerian rotation signature in the Peak PV-diagram, likely because the Keplerian region is found on smaller radii than we can examine with our observations. More sensitive observations will be required to probe the kinematics down to smaller radii to clearly identify a region of Keplerian rotation. We discuss the implications of the detected rotation further in Section 4.

3.5. Sub-arcsecond Resolution SMA Data

We observed BHR7-MMS at the highest resolution available at 1.3 mm from the SMA (0.″6 × 0.″45; 240 AU × 180 AU) to determine if there was evidence of resolved structure on sub-500 AU scales; the inclination of >60° helps simplify the interpretation of the continuum morphology. The SMA continuum image at the highest resolution is shown in Figure 9; this image is produced using only the Very Extended data. The image shows a very strong 1.3 mm detection, that is extended along the minor axis of the beam, orthogonal to the outflow direction (Section 3.8).

The deconvolved size of the continuum source is 0.″52±0.01 × 0.″15±0.04 (208 AU × 60 AU) with a position angle of 91±2°. This is suggestive of a compact, disk-like structure around BHR7-MMS with a radius of $\sim$104 AU, at the assumed distance of 400 pc. If the continuum is tracing a symmetric, geometrically-thin disk, we can estimate the inclination of the

disk by taking the inverse cosine of the minor/major axis obtained from the Gaussian fit deconvolved from the synthesized beam. Note that this method will break down when the source inclination approaches 90° (edge-on) because the disk is not infinitely thin and the inherent thickness will never result in an inclination that is 90°. With these assumptions and caveats in mind, we estimate the system inclination to be 73.2°, which is consistent with the estimates based on the SED and image morphology. The integrated flux-density of the source is 197±2.2 mJy (127±1 mJy peak); these measurements also result from the Gaussian fit. The lower-resolution Compact data are more sensitive to the extended envelope emission and we observe an integrated flux density of 273±49 mJy.

3.6. Mass Estimates from Dust Continuum

The mass of the envelope and compact structure in BHR7 can be estimated using the flux density of the dust continuum emission observed toward it. Under the assumption that the dust emission is optically thin and isothermal, the dust mass is given by

$$M_{dust} = \frac{D^2 F_\lambda}{\kappa_\lambda B_\lambda(T_{dust})}. \tag{1}$$

D is the distance (∼400 pc), F_λ is the observed flux density, B_λ is the Planck function, T_{dust} is the dust temperature, and κ_λ is the dust opacity at the observed wavelength. T_{dust} is assumed to be 30 K, consistent with temperature estimates on ∼100 AU scales (Whitney et al. 2003c) and κ_λ is 0.899, taken from Ossenkopf & Henning (1994). We then multiply the resulting value of M_{dust} by 100, assuming the canonical dust to gas mass ratio of 1:100 (Bohlin et al. 1978).

The flux density from the Very Extended observations of 197±2.2 mJy translates to a mass of 0.42 M$_\odot$ and the flux density from the Compact observations of 273±49 mJy translates to 0.51 M$_\odot$. Because the interferometer is missing some flux, we also calculate the mass from the 1.2 mm SIMBA flux density measurement from SEST. The flux density was 0.76 Jy at 1.2 mm, translating to a mass of 1.2 M$_\odot$, assuming the dust opacity spectral index of ∼1.8 from Ossenkopf & Henning (1994). If we extrapolate the 1.2 mm flux density to 1.3 mm using the dust opacity spectral index of ∼1.8, the SIMBA flux density is ∼0.55 Jy. This means that a bit less than half of the continuum emission is coming from sub-arcsecond scales (radii < 200 AU), as traced by the Very Extended observations, and the rest is coming from the extended envelope. Furthermore, we had assumed a temperature of 30 K in the previous calculations, if the average temperature traced in the SIMBA data was 20 K rather than 30 K, the corresponding mass would be 2.03 M$_\odot$. The *Herschel* 500 µm also traces cold dust from the envelope and if we assume T=20 K and the same dust opacity spectral index,

the mass is calculated to be 1.55 $M_\odot$. The 500 μm data may be more affected by opacity from scales near the disk and this could underestimate the total mass.

3.7. Visibility Amplitude Profile

The visibility amplitude data themselves can also reveal signatures of structure that are not readily apparent in the images. We show the visibility amplitude profile toward BHR7-MMS in Figure 10 for the combined Compact, Extended, and Very Extended datasets. We present three different views of the visibility amplitude data, standard circular averaging, a section of the uv-plane along the major axis of the source (orthogonal to the outflow) and a section along the minor axis of the source (along the outflow). There is a clear envelope component at short uv-distances, where the amplitudes steeply rise and then there is a more slowly declining component from about 30 kλ to 300 kλ. At uv-distances >50 kλ the three points begin to diverge and visibility amplitudes along the major axis decline more rapidly than those along the minor axis; a similar analysis technique was also employed by (Aso et al. 2017). The divergence of the three profiles is indicative of a flattened structure. This trend is evident to uv-distances >200 kλ (scales <1″). There is also signal at the greatest uv-distance we measure, indicating that the structure in BHR7 is not fully resolved. The slowly declining component reflects a more compact structure, possibly a disk.

The imaginary visibility amplitudes also show some structure, a symmetric source would have an imaginary component with zero amplitude. Therefore, we are tracing some asymmetric structure in the envelope down to scales approaching the disk size. However, it is difficult to quantify the nature of the asymmetry with our S/N, but we can further analyze the real component using simple models for envelope and disk structure. In Figure 10, we also overlay model visibility amplitude profiles for several different density structures: a disk with a surface density profile of R^{-1} and radius of 100 AU, an envelope undergoing rotating collapse (Ulrich 1976; Cassen & Moosman 1981) with a centrifugal radius of 100 AU (the density profile inside the centrifugal radius is proportional to $R^{-1/2}$ inside of the centrifugal radius and proportional to $R^{-3/2}$ outside), a power-law envelope with a radial density profile proportional to R^{-2}, and the combination of a disk and the rotating collapse model.

These models are from the same set of Hyperion (Robitaille 2011) models used in Tobin et al. (2015), and we assume that the emission is optically thin such that we can freely scale and combine the two components without re-running the radiative transfer model. The two envelope-only models are scaled to match the point with the smallest uv-distance, but do not contain an embedded disk. This shows that an envelope-only models cannot describe the observational data without a disk component. Even if the envelope-only models were

are scaled up to come closer to matching the small-scale structure, the shape of visibility amplitude profiles are inconsistent with the profile observed from baselines longer than 50 kλ. Thus, the visibility amplitude profile for a 100 AU disk provides the best match to the data.

The data are consistent with an envelope having a centrifugal radius of 100 AU and a mass of 2.1 M$_\odot$, within the envelope an embedded disk with a 100 AU radius and a mass of 0.47 M$_\odot$ is needed to reproduce the visibility amplitude profile. This analysis demonstrates that the data cannot be fit with an envelope-only model, requiring a more compact component that is consistent with a a disk. A self-consistent radiative transfer model of the disk and envelope, as well as the SED, is reserved for future work.

3.8. Outflow

While the near-infrared and *Spitzer* data indicate the presence of an outflow carving out cavities observed in scattered light, the SMA observations provide the first direct measurements of the molecular outflow. The outflow from BHR7-MMS is clearly detected in ^{12}CO and the integrated intensity maps of the red and blue-shifted sides of the outflow at different velocity ranges are shown in Figure 11. The outflow exhibits structure typical for some Class 0 protostars, a wide-angle component at low-velocity and a collimated high-velocity molecular jet (e.g., Hirano et al. 2010). From the orientation of the high-velocity jet, the outflow position angle (PA) is about -5.9° east of north. The PV diagram taken along the outflow is also shown in Figure 11. It shows the significant outflow emission out to ±30 km s^{-1} from the systemic velocity.

The near-infrared and *Spitzer* IRAC images also show two bright knots of shocked molecular line emission. Their peak brightness at 4.5 μm is indicative of the line emission being dominated by shock-excited H$_2$ emission. There is some emission in Ks-band which also contains an H$_2$ line, but it is not as bright and/or peaked as the 4.5 μm emission. This could result from the Ks-band feature being more affected by extinction than the 4.5 μm feature. The outflow knots are located at nearly symmetric positions along the outflow axis. T The northern knot is 11″2 (4480 AU) from the continuum source and the southern knot is 10″75 (4300 AU) from the continuum source.

The maximum observed velocity with respect to the systemic velocity is ~30 km s^{-1}; this is approximate because there may be emission below our sensitivity limit at higher velocities. Correcting this velocity for the approximate inclination of 73.2° the true velocity of the highest velocity outflow is ~104 km s^{-1}. If the H$_2$ knots are traveling along this outflow with the same velocity, their time since ejection is ~205 yr and would be moving

at a rate of $\sim$22 AU yr^{-1} (0$''$.055 yr^{-1}). Thus, the proper motion of these knots should be detectable now or in the near future given that the images presented here were taken in 2008 (IRAC) and 2009 (JHKs).

We examined the outflow for indications of other shock-tracing species. We did detect SO emission, but it is centered toward the protostar position with a slight extension in the outflow direction and only detected at low-velocities. SiO was not detected in our observations. This indicates that the SO emission is not being produced by shocks in the extended outflow and that the outflow shocks are not strong enough to produce detectable SiO emission.

4. Discussion

The data and results presented for BHR7 show a well-developed, isolated protostar system that appears proto-typical in many ways. It has a well-defined outflow-carved cavity that is apparent in scattered light between 1.6 μm and 8 μm, and the outflow is also traced by CO emission, having a low-velocity wide-angle cavity and a narrow, collimated higher-velocity flow that is aligned with the HH-knots apparent in the near-infrared. The features of the outflow strongly resemble other 'proto-type' systems like HH212 and L1448C (e.g., Zinnecker et al. 1998; Lee et al. 2007; Hirano et al. 2010). However, it remains unclear if shock-tracers like SiO are also associated with the jet; SiO was not detected in the current SMA data.

The velocity gradients, likely tracing rotation except at perhaps the largest scales, are exhibited in multiple molecular tracers (N$_2$D$^+$, C^{18}O, ^{13}CO, and H$_2$CO). The C^{18}O and ^{13}CO appear to trace to trace the rotating, infalling envelope while conserving angular momentum, as evidenced by the R^{-1} velocity profile shown in Figure 8. Thus, it bears remarkable similarity to the earlier data on L1527 IRS from the SMA and Nobeyama Millimeter Array (Ohashi et al. 1997; Yen et al. 2013), but BHR7-MMS has a stronger indication of rotation. L1527 IRS, and other sources that also showed conserved angular momentum (and/or rotation) in early data (e.g., VLA 1623, HH212, Lupus MMS3 Murillo et al. 2013; Lee et al. 2014; Yen et al. 2015, 2017) were later found to have rotationally supported disks when viewed at higher resolution and sensitivity.

4.1. Does BHR7-MMS Contain A Rotationally-Supported Disk?

The ^{13}CO, C^{18}O, and H$_2$CO all show indications of rotation in the envelope and the high-resolution ^{13}CO and C^{18}O, show rotation down to 100s of AU scales. The velocity profile also shows conserved angular momentum from 1000s of AU down to 100s of AU. The scales on which we observe rotation are small enough that magnetic braking will not be strong enough to reverse the increasing rotation velocities (e.g., Zhao et al. 2017). Nevertheless, the current spectral line data do not yet have resolution and sensitivity to resolve and firmly identify the Keplerian region.

In addition to the strong rotation of the inner envelope, the SMA continuum observations at $\sim0\rlap{.}''5$ resolution show that the dust emission is resolved orthogonal to the outflow direction with a radius of ~104 AU (deconvolved Gaussian half-width at half maximum). The state at which we observe BHR7-MMS is remarkably similar to L1527 IRS and VLA 1623, where both had resolved dust continuum orthogonal to the outflow and indications of rotation from lower-resolution kinematic data. The analysis presented in Sections 3.5 and 3.7, show that continuum data are consistent with the presence of a disk at the heart of the rotating envelope. However, we cannot conclusively conclude that such a continuum structure is tracing a rotationally-supported disk around the protostar.

The molecular line kinematics do show rotation up to near the radius of the continuum emission. Thus, if the disk is rotationally-supported, we can simplistically estimate the protostar mass by assuming a Keplerian radius. We adopt a Keplerian radius of 120 AU from resolved dust continuum emission discussed in Section 3.5. This radius corresponds to the radius of the 3σ contour and is slightly larger than the deconvolved half-width at half maximum from the Gaussian fit. For a Keplerian radius of 120 AU, we extrapolated the conserved angular momentum power-law, finding a velocity of 2.58 km s^{-1} at the adopted Keplerian radius. We show in Figure 8 that this radius is just beyond the smallest radius detected by the ^{13}CO and C^{18}O data. Using the formula v = (GM/R)$^{0.5}$, we find that with the assumptions outlined above, the protostar mass could be 1.0 $M_\odot$. This estimate incorporates the $\sim73°$ inclination calculated in Section 3.5 from the Gaussian fit to the continuum

This estimate of central protostar mass is contingent upon both the continuum tracing a fully Keplerian disk (which may not be the case). If the true Keplerian disk is smaller, then the protostar mass would be larger; the protostar mass will scale inversely with the Keplerian radius. For example, if the Keplerian radius is actually 60 AU, then the protostar mass would be ~2 M$_\odot$. While there is considerable uncertainty in the protostar mass, estimates substantially above ~1 M$_\odot$ may be overly large considering the bolometric luminosity of 9.3 L$_\odot$.

4.2. Likelihood of Gravitational Instability

The mass of the postulated disk was found to be large from both the isothermal dust mass calculation (M_{disk}=0.42 $M_\odot$) and the visibility amplitude profile analysis (M_{disk}=0.47 $M_\odot$) in Sections 3.5 and 3.7. However, both of these mass estimates assume a gas to dust mass ratio of 100:1, which can evolve (Ansdell et al. 2016), but it is unclear if any reduction of this ratio is expected in the protostellar phase. Assuming that both the M_{disk}=0.42 $M_\odot$ value and M_*=1.0 $M_\odot$ are accurate, we can examine the likelihood of gravitational instability in the disk of BHR7-MMS.

The typical analytic criterion for stability of a rotating system is given by Toomre's Q, calculating the ratio of thermal pressure support and rotation shear to gravity in the form

$$Q = \frac{c_s \Omega}{\pi \Sigma G}. \tag{2}$$

Values greater than 1 indicate that the disk is stable against self-gravity and values less than 1 indicate that the disk is unstable and may be prone to fragmentation.

This equation can be rewritten for a disk (Kratter & Lodato 2016; Tobin et al. 2016) in the form

$$Q \approx 2\frac{M_*}{M_d}\frac{H}{r}. \tag{3}$$

$H = c_s/\Omega$ is the disk scale height, c_s the disk sound speed, and Ω the Keplerian angular velocity. Using the disk and star masses derived above, and a typical disk temperature of 30 K ($c_s = 0.3$ km s^{-1}) at a radius of 50 AU ($\Omega \sim 5.6 \times 10^{-10}$ s^{-1}), $Q \approx 0.4$. We can also see from this equation that Q will scale as $M_*^{0.5}$ from the angular velocity dependence on protostar mass, therefore if the current disk mass is accurate, it is possible that the disk is gravitationally unstable. However, another limiting factor may be the uncertainty in the distance (D) to this protostar because the disk mass from dust emission will scale as D^2, but protostar mass measured from the spectral line emission will scale linearly with distance, making Q scale as $D^{1.5}$. Thus, if BHR7 is somehow a factor of 2 closer than the adopted 400 pc distance, the disk mass will be 4× lower and the protostar mass will be 0.5 $M_\odot$, making Q $\sim$ 1.1. We also note that it is possible that we are underestimating the mass in the disk component if it is optically thick.

Future high-resolution observations will be required to more accurately determine the disk and protostar mass to better assess its likelihood of gravitational instability. Moreover, higher-resolution continuum imaging may directly reveal fragments or spiral structure that has recently been uncovered in disks by ALMA (Tobin et al. 2016; Pérez et al. 2016). Finally, Gaia parallaxes of foreground/background stars will enable the distance of the BHR7 globule to be better constrained.

5. Conclusions

We have characterized the protostar within the isolated dark globule BHR7 from the near-infrared to the submillimeter using data from the CTIO 4m, *Spitzer*, *IRAS*, *Herschel*, SEST SIMBA, and the SMA. We have made the first determination of bolometric luminosity 9.3 $L_\odot$ and bolometric temperature (50.5 K) for this protostar, confirming that it is a Class 0 protostar with a luminosity that is higher than the $\sim$1 $L_\odot$ median in the nearby star-forming regions (Dunham et al. 2014). The near-infrared at Ks-band and *Spitzer* IRAC bands show that the source has a well-defined outflow cavity separated by a dark lane. The outflow cavity is traced by an impressive CO outflow that shows both low-velocity wide-angle emission and a collimated, high-velocity jet that has an axis consistent with observed knots of shocked-excited H_2 gas.

We conducted further submillimeter interferometric observations using the SMA in three configurations to examine both the molecular line emission from the envelope down to near the scale of the disk, as well as the small-scale continuum structure. The ^{13}CO and $C^{18}O$ kinematics indicate clear rotation in the inner envelope and the rotation curve in the the inner envelope is rotating consistent with conserved angular momentum. The SMA continuum observations with $\sim$0$''$.5 resolution resolve the continuum orthogonal to the outflow direction, possibly tracing a disk. The deconvolved size of the continuum indicates that the disk radius may be $\sim$100 AU and have an inclination near 73°. Analysis of the visibility amplitude profile down to sub-arcsecond scales requires the presence of a compact structure other than a power-law or rotationally-flattened envelope. A disk plus a rotationally-flattened envelope can reproduce the visibility amplitude profile The strong envelope rotation, coupled with the resolved continuum image and visibility amplitude profile are possible evidence for a rotationally-supported disk within this system. We estimate the disk mass from the continuum emission to be $\sim$0.32 $M_\odot$ and the gas kinematics (assuming a rotationally supported disk radius of $\sim$120 AU) indicate that the protostar mass could be $\sim$1 $M_\odot$. With these two pieces of information, we calculate Toomre's Q, finding that if the observations reflect a rotationally-supported disk, it may be gravitationally unstable.

Furthermore, H_2CO and N_2D^+ observations from larger radii indicate that the envelope still exhibits a velocity gradient beyond 1000 AU with a gradient direction consistent with the smaller-scale ^{13}CO and $C^{18}O$ emission; this possibly indicates bulk rotation of the outer envelope.

These observations as a whole demonstrate that BHR7 may be an excellent proto-type source for studies of star formation, given its isolation from confusing, external influence and its classic outflow and inner envelope rotation profile. Future observations will reveal whether or not there is indeed a rotationally-supported disk and if it is currently only forming

a single star. However, despite its gifts, the ambiguity of the distance toward BHR7 must be resolved to more firmly characterize its properties, and forthcoming parallax data from Gaia should enable more firm constraints on its distance in the near future.

Facilities: SMA, *Herschel*, *Spitzer*, Blanco (ISPI)

REFERENCES

André, P., Ward-Thompson, D., & Barsony, M. 1993, ApJ, 406, 122

Ansdell, M., Williams, J. P., van der Marel, N., et al. 2016, ApJ, 828, 46

Aso, Y., Ohashi, N., Aikawa, Y., et al. 2017, ArXiv e-prints, arXiv:1707.08697

Bergin, E. A., Ciardi, D. R., Lada, C. J., Alves, J., & Lada, E. A. 2001, ApJ, 557, 209

Bohlin, R. C., Savage, B. D., & Drake, J. F. 1978, ApJ, 224, 132

Bourke, T. L., Hyland, A. R., & Robinson, G. 1995a, MNRAS, 276, 1052

Bourke, T. L., Hyland, A. R., Robinson, G., James, S. D., & Wright, C. M. 1995b, MNRAS, 276, 1067

Caselli, P., Walmsley, C. M., Tafalla, M., Dore, L., & Myers, P. C. 1999, ApJ, 523, L165

Cassen, P., & Moosman, A. 1981, Icarus, 48, 353

Chen, H., Myers, P. C., Ladd, E. F., & Wood, D. O. S. 1995, ApJ, 445, 377

Cieza, L. A., Casassus, S., Tobin, J., et al. 2016, Nature, 535, 258

Codella, C., Cabrit, S., Gueth, F., et al. 2014, A&A, 568, L5

Crapsi, A., Caselli, P., Walmsley, C. M., et al. 2004, A&A, 420, 957

Dunham, M. M., Stutz, A. M., Allen, L. E., et al. 2014, Protostars and Planets VI, 195

Emprechtinger, M., Caselli, P., Volgenau, N. H., Stutzki, J., & Wiedner, M. C. 2009, A&A, 493, 89

Evans, II, N. J., Allen, L. E., Blake, G. A., et al. 2003, PASP, 115, 965

Fazio, G. G., Hora, J. L., Allen, L. E., et al. 2004, ApJS, 154, 10

Fischer, W. J., Megeath, S. T., Furlan, E., et al. 2017, ApJ, 840, 69

Furlan, E., Fischer, W. J., Ali, B., et al. 2016, ApJS, 224, 5

Griffin, M. J., Abergel, A., Abreu, A., et al. 2010, A&A, 518, L3

Hartley, M., Tritton, S. B., Manchester, R. N., Smith, R. M., & Goss, W. M. 1986, A&AS, 63, 27

Hirano, N., Ho, P. P. T., Liu, S.-Y., et al. 2010, ApJ, 717, 58

Ho, P. T. P., Moran, J. M., & Lo, K. Y. 2004, ApJ, 616, L1

Jørgensen, J. K. 2004, A&A, 424, 589

Kämpgen, K. 2002, Master's Thesis

Kämpgen, K., Chini, R., Nielbock, M., & Albrecht, M. 2004, in The Dense Interstellar Medium in Galaxies, ed. S. Pfalzner, C. Kramer, C. Staubmeier, & A. Heithausen, Vol. 91, 405

Kratter, K., & Lodato, G. 2016, ARA&A, 54, 271

Kratter, K. M., Matzner, C. D., Krumholz, M. R., & Klein, R. I. 2010, ApJ, 708, 1585

Langer, W. D. 1985, in Protostars and Planets II, ed. D. C. Black & M. S. Matthews, 650–667

Lee, C.-F., Hirano, N., Zhang, Q., et al. 2014, ApJ, 786, 114

Lee, C.-F., Ho, P. T. P., Hirano, N., et al. 2007, ApJ, 659, 499

Lindberg, J. E., Jørgensen, J. K., Brinch, C., et al. 2014, A&A, 566, A74

Looney, L. W., Tobin, J. J., & Kwon, W. 2007, ApJ, 670, L131

McMullin, J. P., Waters, B., Schiebel, D., Young, W., & Golap, K. 2007, in Astronomical Society of the Pacific Conference Series, Vol. 376, Astronomical Data Analysis Software and Systems XVI, ed. R. A. Shaw, F. Hill, & D. J. Bell, 127

Murillo, N. M., & Lai, S.-P. 2013, ApJ, 764, L15

Murillo, N. M., Lai, S.-P., Bruderer, S., Harsono, D., & van Dishoeck, E. F. 2013, A&A, 560, A103

Ohashi, N., Hayashi, M., Ho, P. T. P., & Momose, M. 1997, ApJ, 475, 211

Ohashi, N., Saigo, K., Aso, Y., et al. 2014, ApJ, 796, 131

Ossenkopf, V., & Henning, T. 1994, A&A, 291, 943

Pérez, L. M., Carpenter, J. M., Andrews, S. M., et al. 2016, Science, 353, 1519

Poglitsch, A., Waelkens, C., Geis, N., et al. 2010, A&A, 518, L2

Robitaille, T. P. 2011, A&A, 536, A79

Sakai, N., Oya, Y., Sakai, T., et al. 2014, ApJ, 791, L38

Santos, N. C., Yun, J. L., Santos, C. A., & Marreiros, R. G. 1998, AJ, 116, 1376

Sault, R. J., Teuben, P. J., & Wright, M. C. H. 1995, in Astronomical Society of the Pacific Conference Series, Vol. 77, Astronomical Data Analysis Software and Systems IV, ed. R. A. Shaw, H. E. Payne, & J. J. E. Hayes, 433

Skrutskie, M. F., Cutri, R. M., Stiening, R., et al. 2006, AJ, 131, 1163

Stutz, A. M., Rieke, G. H., Bieging, J. H., et al. 2009, ApJ, 707, 137

Testi, L., Birnstiel, T., Ricci, L., et al. 2014, Protostars and Planets VI, 339

Tobin, J. J., Hartmann, L., Bergin, E., et al. 2012a, ApJ, 748, 16

Tobin, J. J., Hartmann, L., Calvet, N., & D'Alessio, P. 2008, ApJ, 679, 1364

Tobin, J. J., Hartmann, L., Chiang, H.-F., et al. 2012b, Nature, 492, 83

Tobin, J. J., Hartmann, L., & Loinard, L. 2010a, ApJ, 722, L12

Tobin, J. J., Hartmann, L., Looney, L. W., & Chiang, H. 2010b, ApJ, 712, 1010

Tobin, J. J., Hartmann, L., Looney, L. W., & Chiang, H.-F. 2010c, ApJ, 712, 1010

Tobin, J. J., Hartmann, L., Chiang, H.-F., et al. 2011, ApJ, 740, 45

Tobin, J. J., Bergin, E. A., Hartmann, L., et al. 2013, ApJ, 765, 18

Tobin, J. J., Dunham, M. M., Looney, L. W., et al. 2015, ApJ, 798, 61

Tobin, J. J., Kratter, K. M., Persson, M. V., et al. 2016, Nature, 538, 483

Ulrich, R. K. 1976, ApJ, 210, 377

van der Bliek, N. S., Norman, D., Blum, R. D., et al. 2004, in Proc. SPIE, Vol. 5492, Ground-based Instrumentation for Astronomy, ed. A. F. M. Moorwood & M. Iye, 1582–1589

Vorobyov, E. I., & Basu, S. 2006, ApJ, 650, 956

Whitney, B. A., Wood, K., Bjorkman, J. E., & Cohen, M. 2003a, ApJ, 598, 1079

Whitney, B. A., Wood, K., Bjorkman, J. E., & Wolff, M. J. 2003b, ApJ, 591, 1049

—. 2003c, ApJ, 591, 1049

Woermann, B., Gaylard, M. J., & Otrupcek, R. 2001, MNRAS, 325, 1213

Yen, H.-W., Koch, P. M., Takakuwa, S., et al. 2015, ApJ, 799, 193

—. 2017, ApJ, 834, 178

Yen, H.-W., Takakuwa, S., Ohashi, N., & Ho, P. T. P. 2013, ApJ, 772, 22

Zhao, B., Caselli, P., Li, Z.-Y., & Krasnopolsky, R. 2017, ArXiv e-prints, arXiv:1706.06504

Zinnecker, H., McCaughrean, M. J., & Rayner, J. T. 1998, Nature, 394, 862
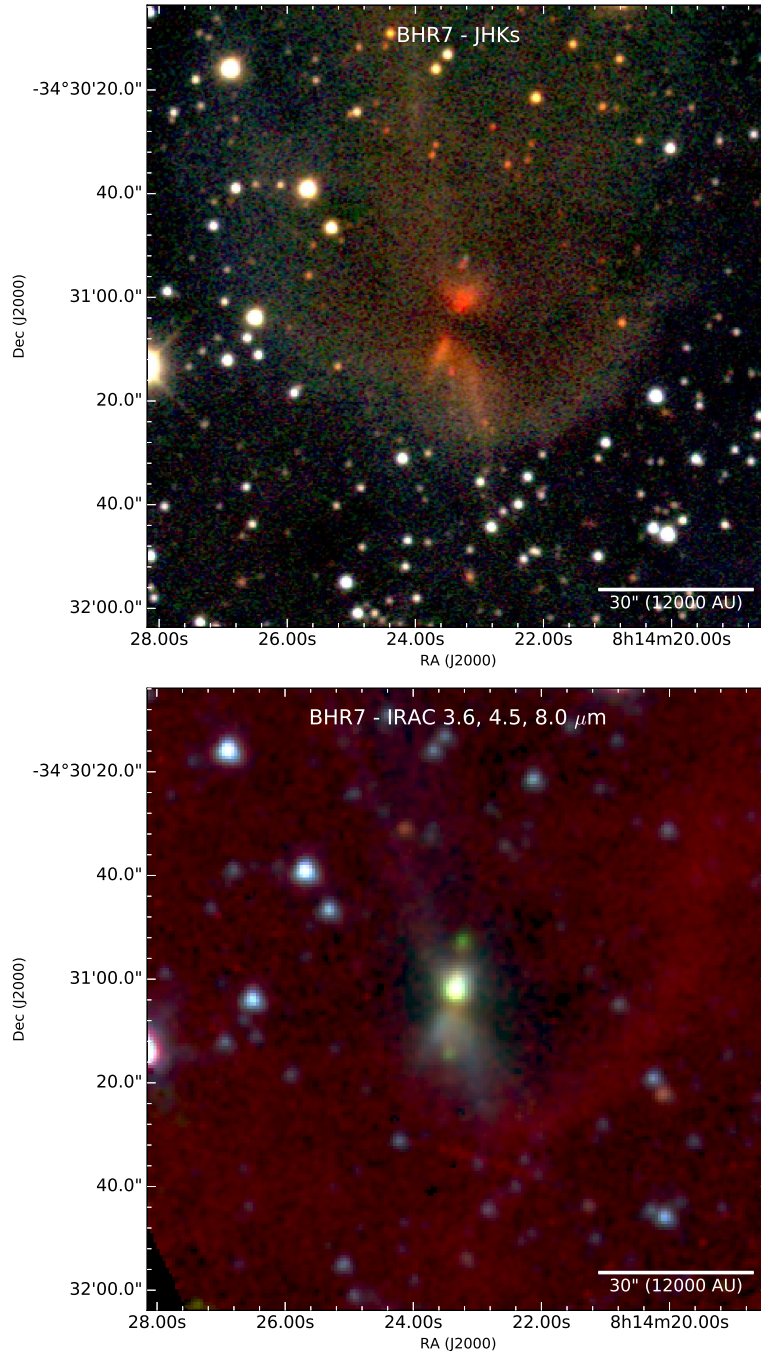
Fig. 1.— Images of BHR7 at J, H, and Ks-bands (top) and *Spitzer* IRAC 3.6, 4.5, 8.0 μm (bottom); the wavelength order for both images are assigned to blue, green, and red colors, respectively. Notice the thick dark lane separating the north and south sides of the outflow cavity in both images. The outflow cavity appears in scattered light in nearly the north-south direction. There are also two knots in the center of the outflow cavity that are prominent in Ks-band and at 4.5 μm, tracing a shock in the outflow. The dark lane appears thicker at JHKs-bands due to greater levels of extinction and it also has a slightly different angle. There also appears to be an 'edge' to the envelope surrounding BHR7, appearing in diffuse scattered light at JHKs-bands, but also in 8 μm, likely reflecting PAH emission.
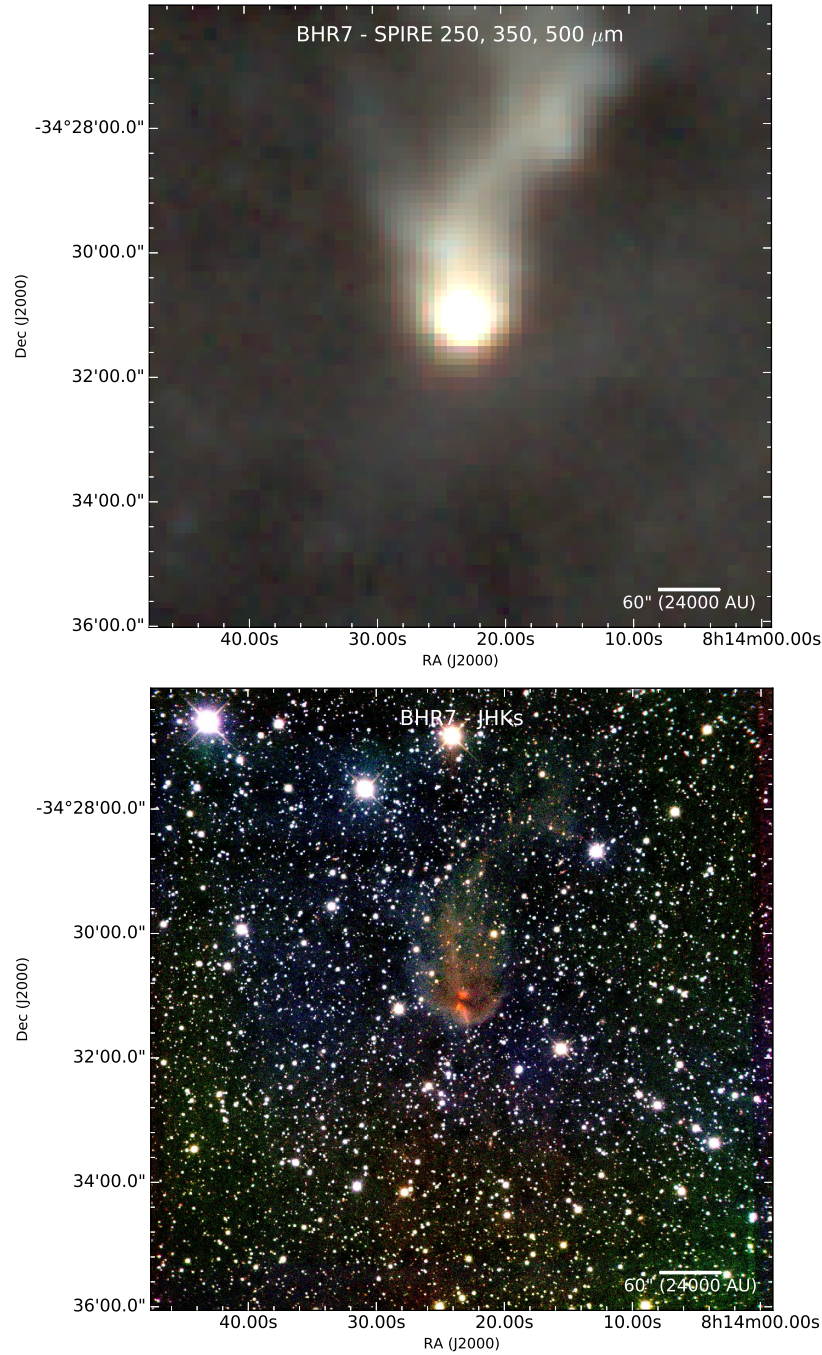
Fig. 2.— *Herschel* SPIRE image at 250, 350, and 500 μm (top) and a wider-field J, H, and Ks image (bottom); the color ordering of the wavelengths is blue, green, and red, respectively. The SPIRE image shows the extended cloud and the dense core at the base where the protostar is forming. Some of the extended SPIRE emission has corresponding diffuse scattered light in the near-infrared as shown in the JHKs image.
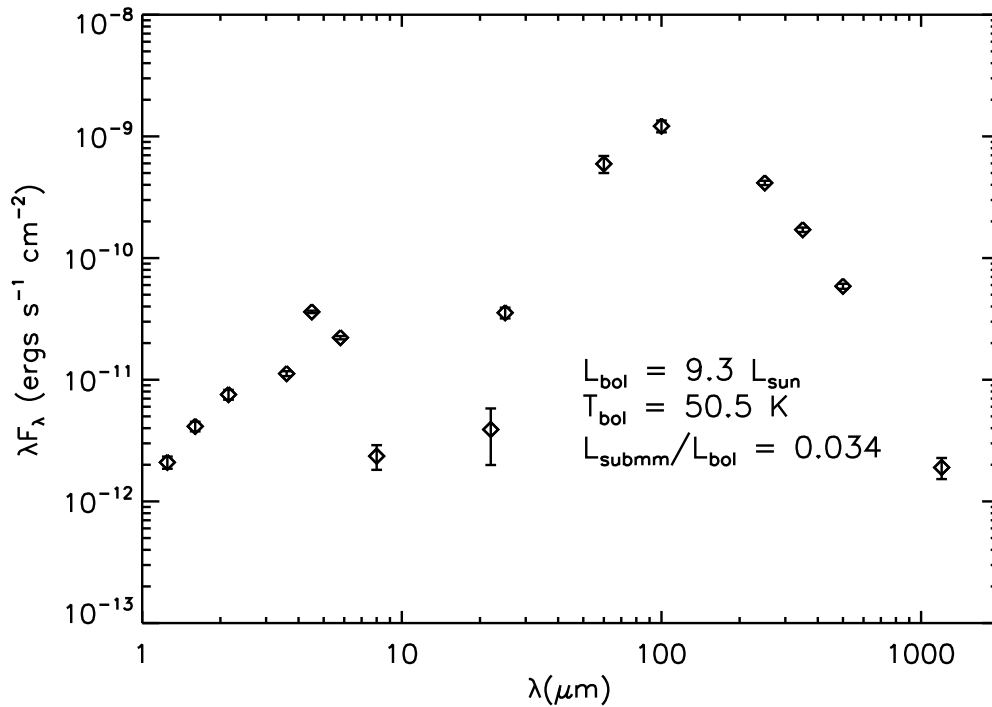
Fig. 3.— Spectral Energy Distribution for BHR7. The 3.6 to 8.0 μm measurements are from *Spitzer* IRAC, the 25 to 100 μm measurements are from IRAS, the 250 - 500 μm measurements are from *Herschel* SPIRE, and the 1.2 mm datapoint is from SEST SIMBA. From these data, we measured a bolometric luminosity of 9.3 $L_{\odot}$ and a bolometric temperature of 50.5 K. The ratio of submillimeter luminosity to bolometric luminosity of 0.034 meets criteria for a Class 0 protostar (>0.005; André et al. 1993).
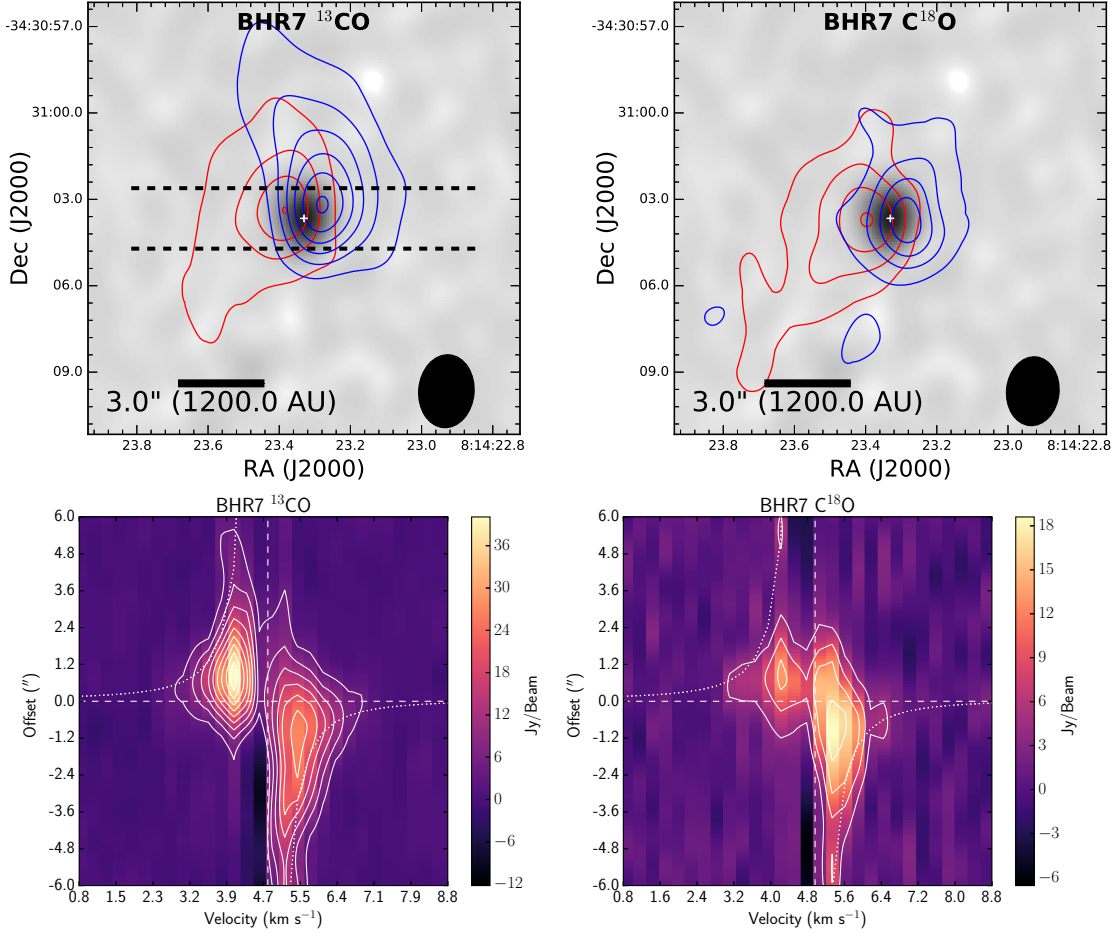
Fig. 4.— BHR7 ^{13}CO and C^{18}O blue and red-shifted integrated intensity maps (top panels) for the combination of SMA Extended and Compact observations, overlaid on the continuum imaging from Extended configuration (grayscale). The two CO isotopologues both clearly show a velocity gradient in the east-west direction, nearly orthogonal to the outflow PA. The dashed lines overlaid on the ^{13}CO integrated intensity map denotes the region used for the PV diagram extraction for both ^{13}CO and C^{18}O (12″ length, 2″.1 width). The PV diagrams are shown for the ^{13}CO and C^{18}O (bottom panels), with a Keplerian rotation curve drawn for a 1.0 M$_\odot$ star. The dashed lines mark the source position and system velocity. The beams for the ^{13}CO and C^{18}O observations are 2″.53×1″.92 and 2″.39×1″.82, respectively. For the ^{13}CO, the red contours start at 5.0σ and increase by 7.5σ and the blue contours start at 10.0σ and increase by 10.0σ, where σ_{red}=0.19 K km s^{-1} and σ_{blue}=0.18 K km s^{-1}. Then for the C^{18}O, the contours start at and increase on 5σ intervals; σ_{red}=0.18 K km s^{-1} and σ_{blue}=0.2 K km s^{-1}.
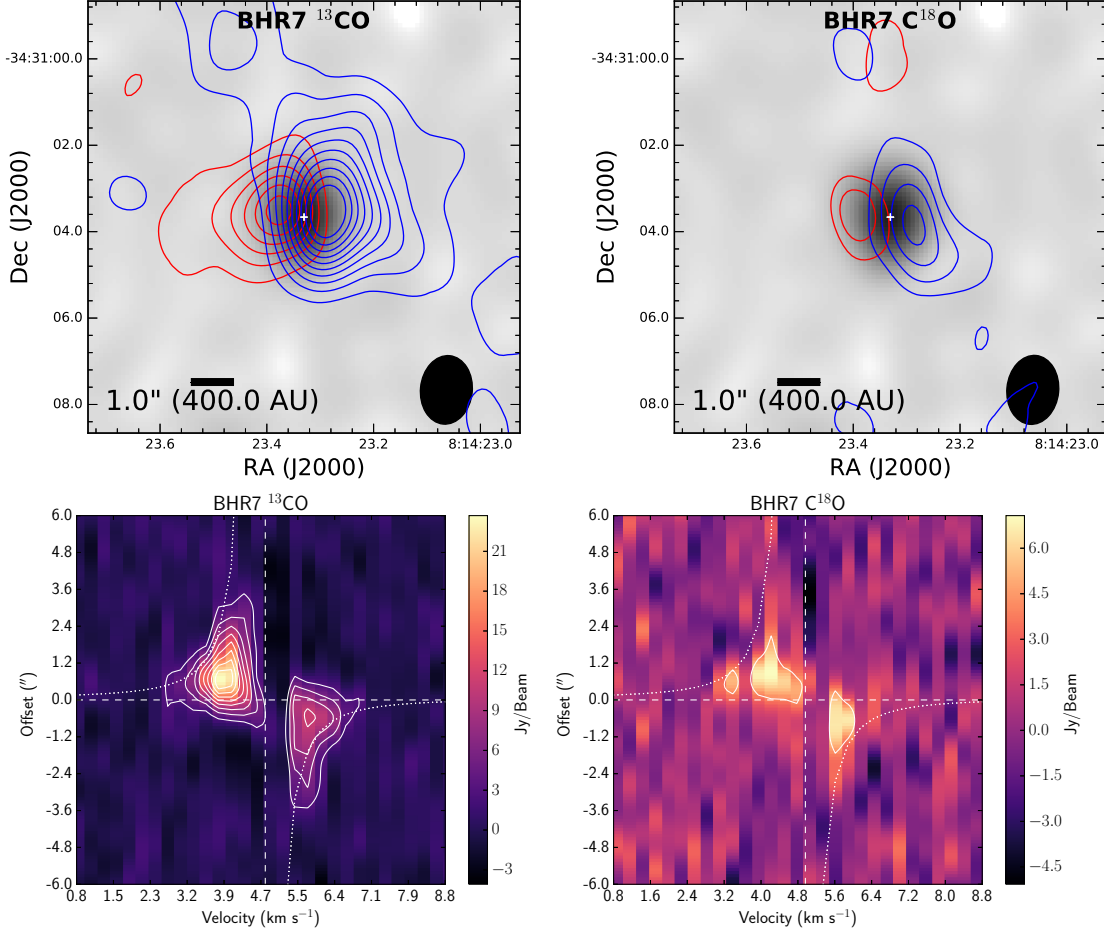
Fig. 5.— BHR7 ^{13}CO and C^{18}O blue and red-shifted integrated intensity maps from the SMA Extended configuration only (upper panels), overlaid on the continuum imaging from extended configuration (grayscale). Like the lower resolution data, both ^{13}CO and C^{18}O trace a smaller-scale velocity gradient orthogonal to the outflow direction, centered on the continuum position. The PV diagrams shown in the bottom panels for the ^{13}CO and C^{18}O are extracted using the same region in Figure 4, with a Keplerian curve for a 1.0 M$_\odot$ star drawn (dotted line). The dashed lines mark the source position and system velocity. The beams for the ^{13}CO and C^{18}O observations are both $1''6 \times 1''2$. For the ^{13}CO, the red and blue contours start at and increase by 3.0σ, where σ_{red}=0.43 K km s^{-1} and σ_{blue}=0.51 K km s^{-1}. Then for the C^{18}O, the red contours start at 3σ and increase by 2σ, and the red contours start at 3σ and increase by 1σ; σ_{red}=0.52 K km s^{-1} and σ_{blue}=0.63 K km s^{-1}.
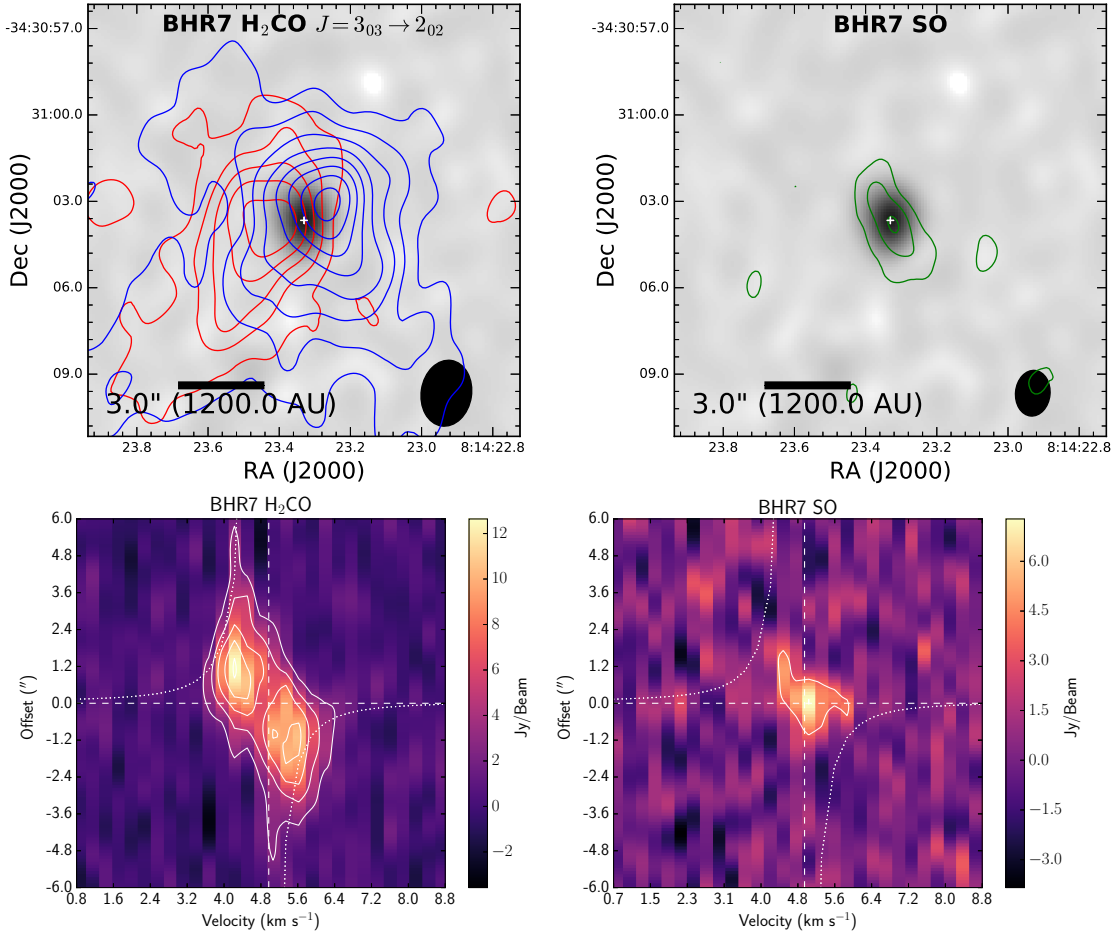
Fig. 6.— SMA H_2CO (upper left) and SO (upper right) integrated intensity contours overlaid on the 1.3 mm continuum (grayscale). The H_2CO is a combination of Extended and Compact observations, while the SO is Extended configuration only. The H_2CO clearly shows a velocity gradient, in the same sense as the CO isotopologues, but with an apparent position angle that is slightly larger. The SO emission is compact and a clear blue and red-shifted separation is not evident at this resolution and sensitivity. The PV diagrams shown for H_2CO and SO (bottom panels) are extracted using the same region shown in Figure 4 with a Keplerian curve for a 1.0 $M_\odot$ star drawn (dotted line). The H_2CO does not strongly trace the higher velocities of the inner envelope, but H_2CO does trace the infalling/rotating envelope beyond the extent of the ^{13}CO and $C^{18}O$ emission very well. The SO appears compact in velocity space. The dashed lines mark the source position and system velocity. The H_2CO beam is $2\farcs3 \times 1\farcs75$ and the SO beam is $1\farcs6 \times 1\farcs2$. The SO contours start and increase on 3σ intervals where $\sigma = 0.7$ K km s^{-1}. For the H_2CO, the contours start and increase on 3σ intervals and $\sigma_{red,blue} = 0.18$ K km s^{-1}.
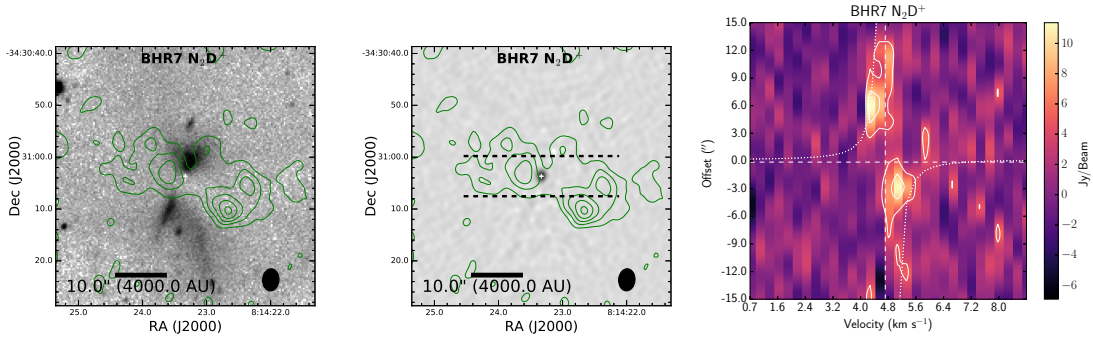
Fig. 7.— SMA N_2D^+ ($J = 3 \rightarrow 2$) observations from combination of Extended and Compact observations; however, the data are tapered to the resolution of the compact configuration to increase the sensitivity to large structures. The left panel shows the N_2D^+ integrated intensity contours overlaid on the Ks-band image, highlighting the coincidence of the thick dark lane. The middle panel shows the N_2D^+ integrated intensity contours overlaid on the 1.3 mm continuum. The N_2D^+ emission is tracing the cold outer envelope where CO is frozen-out and formation of H_2D^+ and N_2D^+ is efficient. The peaks of the N_2D^+ emission are off the continuum source, as expected for a protostellar system with significant internal heating. The PV diagram for N_2D^+, shown in the far right panel, is extracted along the same position angle denoted by the dashed lines in the middle panel ($20''$ length, $7\rlap{.}''75$ width). The PV diagram also shows a large-scale velocity gradient in the envelope surrounding BHR7, possibly tracing rotation on scales outside H_2CO and CO isotopologue emission. The beam is $4\rlap{.}''3 \times 3\rlap{.}''2$ and the contours start at and increase on 2σ intervals where σ=0.1 K km s^{-1}.
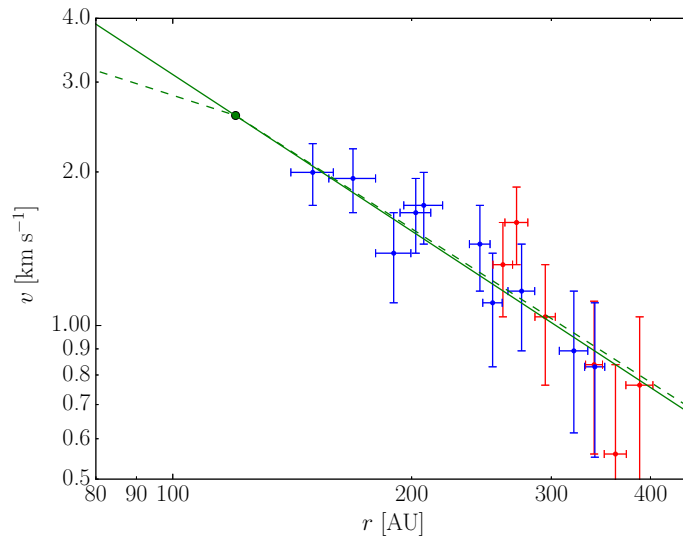
Fig. 8.— The Peak PV diagram of BHR7-MMS including the fitted power law (solid green line) using ^{13}CO and C^{18}O data. The fit to the power-law is -1.02$\pm$0.04 and thus consistent with conservation of angular momentum (v $\propto$ r^{-1}) The dashed line shows a broken power law assuming the break point at 120 AU, 2.58 km s^{-1}, which is denoted by a green dot. With the adopted break point of 120 AU the inferred mass of the protostar is ~1 $\pm$0.4 M$_\odot$. Red data points are red shifted, blue data points are blue shifted with respect to the source velocity.
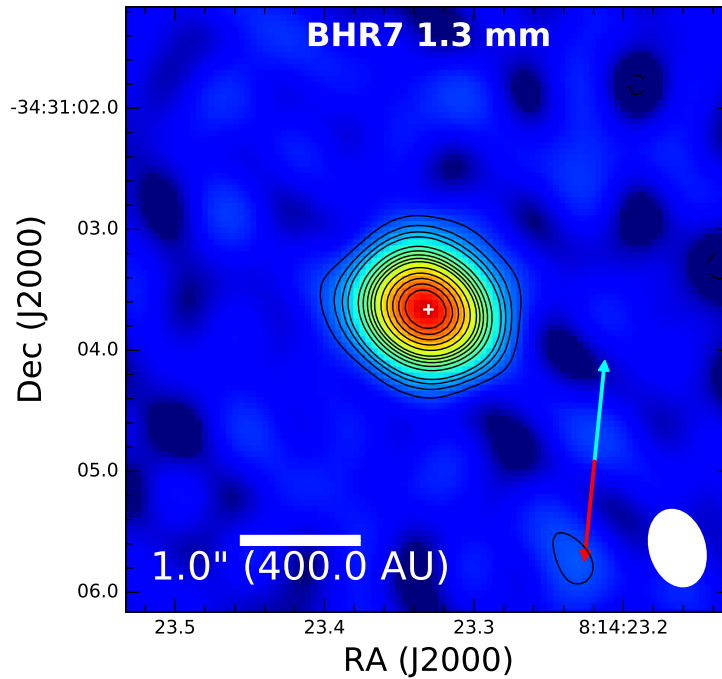
Fig. 9.— SMA 1.3 mm continuum image of BHR7-MMS from Very Extended configuration. The image shows a resolved dust continuum source embedded within BHR7. The source is clearly extended orthogonal to the outflow direction, marked by the blue and red arrows. The width of the continuum source is substantially wider than the minor axis of the 0″.6 × 0″.45 (240 AU × 180 AU) beam. The deconvolved size of the continuum source is 0″.52±0.01 × 0″.15±0.04 (208 AU × 60 AU) with a position angle of 91±2°. This is indicative of a compact, disk-like structure in BHR7.
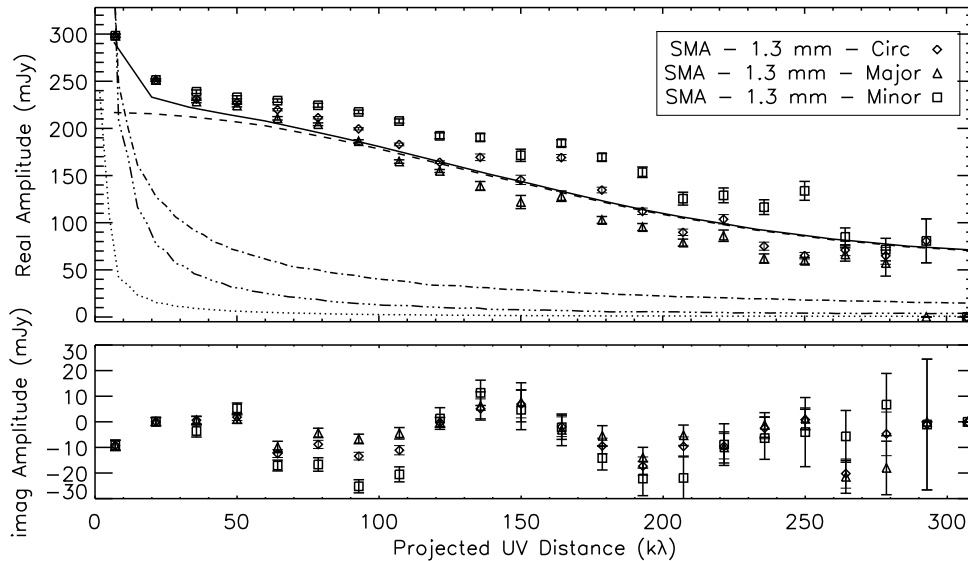
Fig. 10.— Visibility amplitudes from the combined Compact, Extended, and Very Extended datasets. We show both the circularly averaged visibility amplitudes and cuts in the uv-plane along the major and minor axis of the envelope. The major axis decreases more rapidly, demonstrating that the system is more compact along the direction of the outflow than along the equatorial plane of the disk. We overlay visibility amplitudes from radiative transfer models of a rotating, infalling envelope (dotted line) (Ulrich 1976; Cassen & Moosman 1981) and a 100 AU disk, having a surface density profile proportional to R^{-1} (dashed line). The combination of these two components is shown as the solid line. Assuming that all the emission is optically thin, the data are consistent with a 1.57 $M_\odot$ envelope and a 0.47 $M_\odot$ disk. We also overlay an infalling envelope with a volume density profile proportional to R^{-2} (dot-dashed line) and a rotationally-flattened envelope (triple-dot-dashed line). Both envelope models do not have an embedded disk included and they were scaled to match the shortest visibility amplitude. The imaginary plot on the bottom show some hints of possible non-axisymmetry (systematically non-zero values) but at low S/N.
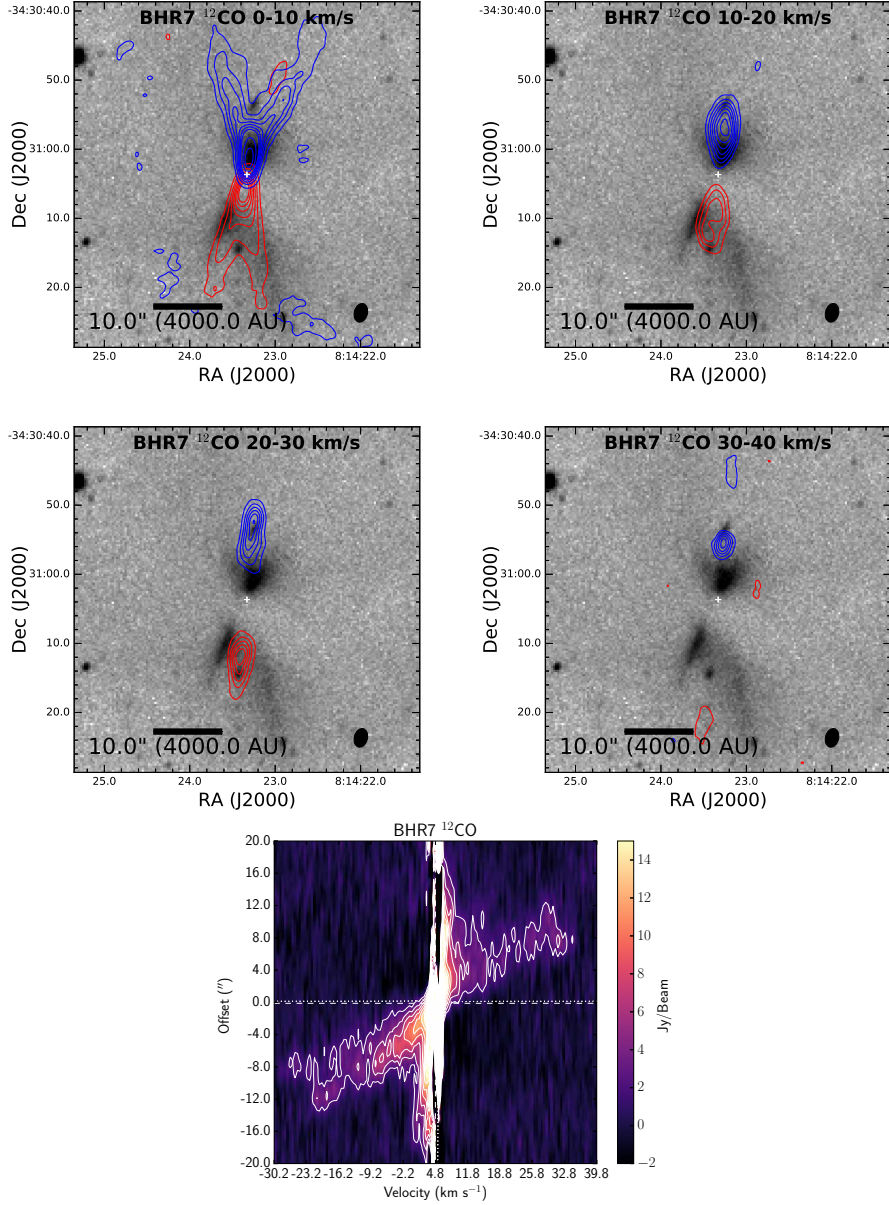
Fig. 11.— SMA ^{12}CO integrated intensity contours in multiple velocity ranges overlaid on the Ks-band near-infrared image. The outflow clearly shows evidence for both a wide-angle ($0-10$ km s^{-1}) and a collimated high-velocity outflow (>10 km s^{-1}). The high-velocity features also coincide with the knots of H$_2$ emission within the outflow cavity that are consistent with shocks. The bottom-most panel shows a position-velocity diagram extracted along the outflow axis, averages in an strip with an angular width of 10.″25. The beam is drawn in the lower right corner of each panel and is 2.″75×1.″91. The contours in the $0-10$ km s^{-1} panel start at 5.0σ and increase in 7.5σ intervals; σ_{red}=0.39 K and σ_{blue}=0.38 K km s^{-1}. For the $10-20$ km s^{-1} and $20-30$ km s^{-1} panels, the contours start at and increase at 5σ where $\sigma_{red,blue}$=0.42 K km s^{-1}. Lastly, for the $30-40$ km s^{-1} panel the contours start at 4σ and increase at 2σ intervals where $\sigma_{red,blue}$=0.42 K km s^{-1}.

Table 1.   SMA Observations

Source	RA (J2000)	Dec (J2000)	Config.[a]	Date (UT)	Calibrators (Gain, Flux)
BHR7	8:14:23.326	-34:31:05.7	VEX	28 Jan 2015	0747-311, Callisto
BHR7	8:14:23.33	-34:31:03.7	COMP	25 Dec 2015	0747-331, Uranus
BHR7	8:14:23.33	-34:31:03.7	EXT	02 Apr 2016	0747-311, Ganymede

[a] VEX - Very Extended, EXT - Extended, and COMP - Compact

Note. — The position listed for VEX corresponds to the phase center of the observations, not the coordinates of the continuum emission, and the positions for EXT and COMP are centered on the continuum source.

Table 2.   BHR7 Photometry

Wavelength (μm)	Flux Density (Jy)	Reference
1.25	0.00087 ± 0.00008	1
1.6	0.0022 ± 0.0002	1
2.15	0.0054 ± 0.0005	1
3.6	0.031 ± 0.001	1
4.5	0.066 ± 0.002	1
5.8	0.044 ± 0.002	1
8.0	0.027 ± 0.003	1
25.0	0.296 ± 0.03	IRAS
60.0	11.9 ± 1.9	IRAS
100.0	40.5 ± 4.5	IRAS
250.0	34.56 ± 1.4	1
350.0	19.95 ± 0.84	1
500.0	9.78 ± 0.47	1
1200.0	0.76 ± 0.15	1

Note. — **The uncertainties listed are statistical only and do not include systematic uncertainty from the absolute flux calibration accuracy. Furthermore, emission in the SPIRE bands is extended beyond the radius for which we measure it.** References: (1) This work.